



Cite this: *Green Chem.*, 2022, **24**, 5125

## Elucidating the role of reactive nitrogen intermediates in hetero-cyclization during hydrothermal liquefaction of food waste†‡

Heather O. LeClerc,<sup>a</sup> Rasha Atwi,<sup>b</sup> Sydney F. Niles,<sup>c</sup> Amy M. McKenna,<sup>c,d</sup> Michael T. Timko,<sup>a</sup> Richard H. West<sup>b</sup> and Andrew R. Teixeira<sup>\*a</sup>

Hydrothermal liquefaction (HTL) has emerged as a promising strategy for converting abundant, water-rich organic streams into an energy-dense, sustainable, biocrude. Despite major strides in improving oil yields and process intensification, a key underlying challenge persists in relating the composition of the feedstock to the ultimate fate of nitrogen, which is especially important for biocrude quality. To elucidate how nitrogen partitions into the respective gas, aqueous, oil and solid hydrothermal products, food waste was treated under HTL conditions (15 wt% solids, 575 K reaction temperature, and 1 hour reaction time) and elemental, chromatographic and mass spectroscopy analyses were performed on the products to establish dominant product classes and to close mass, carbon, and nitrogen balances. Liquid products (aqueous and biocrude) were found to contain nearly 60% of the nitrogen, with a majority of the biocrude-phase nitrogen in the form of amides. *Ab initio* thermodynamic and kinetic simulations on model reactants were used to evaluate potential reaction pathways involving reactive nitrogen intermediates. A subsequent kinetic model was evaluated at reaction temperatures ranging 300–1000 K and for a range of feedstock compositions to identify primary reaction pathways. The Maillard reaction is revealed to be the dominant pathway for converting reactive nitrogen intermediates into observed products, especially those in which nitrogen is present as a heterocyclic aromatic. Subsequent product analysis by Fourier Transform Ion Cyclotron Resonance Mass Spectrometry (FT-ICR MS) confirms strong agreement among the experimental data, kinetic model and proposed Maillard pathways.

Received 24th March 2022,  
Accepted 10th May 2022

DOI: 10.1039/d2gc01135b

rsc.li/greenchem

## Introduction

The current world reliance on fossil fuels and the corresponding environmental impacts have created global interest in alternative, sustainable energy sources. Particularly attractive are approaches that leverage renewable, distributed inputs to sustainably produce liquid fuels and chemicals. Hydrothermal

liquefaction (HTL) has emerged as a promising candidate for converting water-rich mixed organic streams into biocrudes without extensive energy-intensive pretreatment. Processing water-rich feeds is typically challenging for thermal processes but is ideal for hydrothermal methods.<sup>1</sup> HTL's high level of feedstock flexibility<sup>2,3</sup> and the ability to directly produce a liquid biocrude has contributed to a recent surge of interest.<sup>3–5</sup> HTL biocrude production has been demonstrated for algal, lignocellulosic, and waste feedstocks (Table 1) with energy recoveries ranging from 30–60%.<sup>6–8</sup> Despite algae providing greater yields and energy recovery than other feeds, the high cultivation cost and ash content limit its effectiveness and have motivated research into HTL processing of biomass waste, sewage sludge, and food waste feeds.<sup>9–11</sup>

Municipal waste streams (sewage sludge, food waste) are widely available, low-cost feeds that are rich in carbon.<sup>6,10,12,13</sup> Their water content precludes thermal conversion methods, other than hydrothermal ones. Use of waste feedstocks is economically and environmentally friendly due to low, potentially negative, cost and because the energy content of these feeds would otherwise not be used productively.<sup>12,14,15</sup>

<sup>a</sup>Department of Chemical Engineering, Worcester Polytechnic Institute, 100 Institute Road, Worcester, MA, 01609, USA. E-mail: arteixeira@wpi.edu

<sup>b</sup>Department of Chemical Engineering, Northeastern University, 360 Huntington Avenue, 201 Cullinane, Boston, MA, 02115, USA

<sup>c</sup>National High Magnetic Field Laboratory, 1800 Paul Dirac Dr, Tallahassee, FL, 32310, USA

<sup>d</sup>Department of Soil & Crop Sciences, Colorado State University, Fort Collins, CO 80523, USA

† All FT-ICR MS spectra are provided via Open Science Framework <https://osf.io/64bmt/> through DOI: 10.17605/OSF.IO/64BMT.

‡ Electronic supplementary information (ESI) available: GC-MS, FT-ICR MS, and GC × GC methodology. Sensitivity analysis calculations and results, as well as molecule names and chemical classes for all species used in the model. See DOI: <https://doi.org/10.1039/d2gc01135b>

**Table 1** Biochemical composition and proximate analysis of common HTL feedstocks: algae, food waste, and sewage sludge

Feedstock	Proximate analysis (%)					C (%)	H (%)	N (%)	O (%)	Source
	Protein	Carb.	Lipid	Ash	Moisture					
Algae	7–63	9–54	13–55	4–22	65–80	50–62	7–10	1–10	17–35	Shakya <i>et al.</i> <sup>16</sup>
Food waste	4–22	40–70	6–24	0–6	61–86	40–60	6–10	1–6	25–55	Paritosh <i>et al.</i> <sup>17</sup>
Sewage sludge	2–42	25–52	0.1–41	2–34	70–90	35–50	5–9	3–8	33–60	Chen <i>et al.</i> <sup>1</sup>

Unfortunately, the heteroatom content of waste feeds, especially nitrogen, reduces biocrude quality and possibly yields.<sup>12,14,15</sup>

To obtain a high-quality oil product, substantial efforts must be made to minimize oil-phase heteroatom (N, O, S) content. HTL input streams can contain anywhere between 1 and 10 wt% nitrogen for woody biomass and high-protein algae, and >50 wt% oxygen.<sup>18,19</sup> Oxygen is typically found in the aqueous and gas phases in near equal amounts, whereas as much as 50% of the nitrogen present in the feed appears in the biocrude as a contaminant that must be removed by subsequent treatments.<sup>20</sup> Nitrogen removal is conventionally more difficult than oxygen removal, and removing nitrogen heterocycles is especially challenging.<sup>21–23</sup> Moreover, nitrogen interferes with catalytic acid sites intended for oxygen and sulfur removal, further complicating upgrading efforts.<sup>24</sup> Minimizing the nitrogen upstream in the feed or in the biocrude formed during hydrothermal processing is preferred over removing it during biocrude upgrading. In the hydrothermal step, it would be particularly advantageous to selectively control the fate of

nitrogen—namely to be able to partition it into the gaseous, solid or aqueous phases, leaving the primary biocrude phase nitrogen-free. Our current knowledge of the chemical pathways that result in these respective fates, however, are substantially lacking with regard to the role of nitrogen in these reactive mixed feeds.

To better understand these pathways, thermodynamic and kinetic simulations are required. *Ab initio* calculations have been used on biopolymeric systems to understand key degradation steps during lignin depolymerization<sup>25,26</sup> and to reveal primary homolytic cleavage pathways during cellulose pyrolysis.<sup>27</sup> Notably, however, these studies are typically constrained to the primary reactions of single component, well-ordered feeds or surrogates that are not able to capture the more reactive secondary couplings of oligomeric, mixed component solvated environment that is prevalent during hydrothermal waste processing.

Current knowledge regarding HTL mechanisms are limited to lumped kinetic studies which rely on gas chromatography and mass spectrometry (GC-MS) analysis.<sup>8,28–30</sup> While this

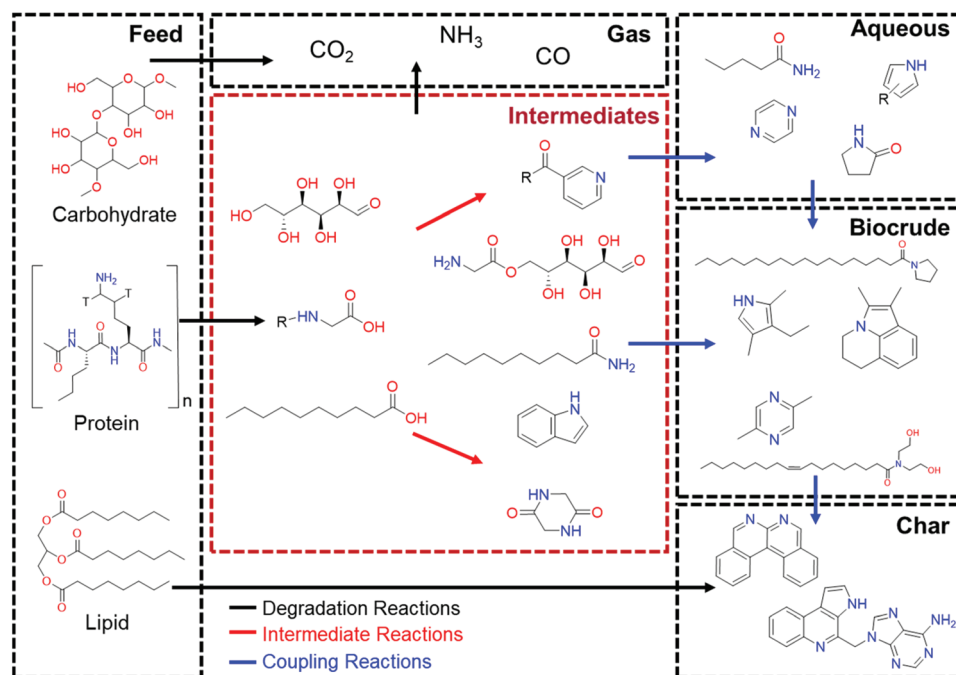


**Fig. 1** Representative nitrogen pathways for hydrothermally depolymerizing macromolecules of food waste and algae to reactive intermediates which form secondary condensation products before ultimately condensing to form biocrudes, and chars. This paper focuses on understanding the condensed phase chemistry in the reactions of intermediates (red dashed box).

approach has proven valuable in providing insight into product phase distributions and general nitrogen pathways, it fails to describe the highly reactive condensed phase environment and particularly, the molecular-level intermediate pathways and barriers for driving nitrogen to each product phase.<sup>8,31,32</sup> When considering food waste decomposition, it is typically considered to progress through two consecutive stages (Fig. 1). In the first, the biopolymers (starches, proteins, fats) are hydrolytically decomposed into short-chained oligomers and monomers.<sup>11</sup> These small, solvated molecules are then free to couple in increasing degrees to form the aqueous (light), oil (heavy) and solid (char) products. With this perspective, the focus of the current study is not to understand the first decomposition stage. Instead, it is to better understand how the small degradation products build back up to form the biocrude, and specifically how the nitrogen functionality, primarily from the proteins, becomes incorporated into the biocrude.

The composition of the reactive intermediate mixture is derived from detailed chemical analysis of the product fractions. The biocrude alone may contain thousands of unique compounds,<sup>33–35</sup> causing analytical challenges, particularly with conventional GC-MS which provide molecular-level precision for volatile biocrude components but is not sufficient for the significant portion of the biocrude that is not volatile enough for GC analysis.<sup>36</sup> Fourier-Transform Ion Cyclotron Resonance Mass Spectrometry (FT-ICR MS) can provide molecular formula with isotopic accuracy on a molecular basis across the entire molecular weight regime of the product oil and is a promising technique for biocrude analysis.<sup>34,35,37</sup> While FT-ICR MS has been used to advance scientific understanding of molecular pathways in pyrolysis of biomass,<sup>38–41</sup> its application to biocrude analysis – and especially to pathway discovery – is much more limited.<sup>34,42</sup> A combination of GC-MS and FT-ICR MS along with the known initial feed structures are used in this study to carefully select key functionality to be incorporated into chemical surrogates to be used in DFT studies to evaluate intermediate reaction pathways.

This work will examine the role of feedstock composition and temperature on the type and amount of HTL product nitrogen. An analysis of small, volatile molecules found in food waste HTL biocrude will serve to identify important molecular classes which will be used to develop a reaction network for use in thermodynamic and kinetic simulations. The simulation results will then be compared to large biocrude molecules identified *via* FT-ICR MS to ensure model validity. The results of this work aim to assist in understanding nitrogen heterocycle formation at hydrothermal liquefaction conditions to make recommendations for optimal feedstock-specific operating conditions.

## Materials & methods

### Development of reaction mechanism

Reaction mechanisms were formed capturing the interactions of the three primary components of non-woody biomass, *i.e.*,

protein, lipid, and carbohydrates. To maximize computational efficiency, simple model compounds were chosen. Glycine, the smallest amino acid, was chosen as a model protein degradation product; butadiene as the model fatty acid; and various small aldehydes (formaldehyde, glyoxal, furfuraldehyde, and glyceraldehyde) were used as model carbohydrate decomposition products. Glyceraldehyde was specifically chosen due to its known reactivity during the Maillard reaction.<sup>43,44</sup> HTL reaction mechanisms were identified from various experimental studies which involved identification of specific compounds resulting from macromolecular interactions.<sup>42,45–49</sup> Reactions were chosen to represent Maillard, hydrodenitrogenation and Aza Diels Alder (ADA) reactions to ensure representative understanding of the types of nitrogen reactions. These reactions were then divided into schemes based on the type and number of reactants involved.

### Electronic structure calculations

Quantum chemical calculations were completed with the Gaussian 16 program suite. All chemical species are calculated in their singlet state and gas phase. The composite method CBS-QB3 was used to optimize geometries and evaluate single-point energies. Force constants and vibrational frequencies were calculated with B3LYP/CBSB7. The torsional motion around the single bonds in each molecule were treated as hindered internal rotations where each angle corresponding to an internal rotation was varied in incremental steps of 10° for 36 steps to achieve complete rotation, allowing other coordinates to relax, evaluated with B3LYP/6-31G(d,p). Transition states were also calculated using CBS-QB3, with frequency calculations performed to verify the existence of only one imaginary frequency per transition state. When necessary, additional optimizations were performed to ensure the result was the lowest energy transition state. All calculations (optimization, frequency, and hindered rotor scans) were repeated using the density functional theory method M06-2X/6-31G+(d,p) for comparison but the results presented here are from CBS-QB3, apart from Scheme 4 reaction 3 because species M<sub>29</sub> and transition state 4.3 could not be calculated at CBS-QB3 on the available computer hardware.

As water is the solvent and thus in extreme excess, it is taken to be pseudo zeroth order in all kinetic expressions. This is further confirmed by sensitivity analysis (Fig. S4†) which shows little sensitivity to changes in water concentration. Solvent effects can have significant impacts on some reaction rates, especially when reactants or products have strong interactions with the solvent, *e.g.* are hydrophobic or form hydrogen bonds.<sup>50</sup> For example, Bini *et al.*<sup>51</sup> reported an increase in Diels Alder reaction rate in aqueous media, whereas Baisier *et al.*<sup>52</sup> also found an increase in Maillard reaction rates in the presence of water with an excess of sugar, representing the two primary reaction types explored in this work. Furthermore, some reactions can be catalyzed by an explicit interaction with a solvent molecule. These effects are necessarily neglected in the current calculations, but the presumption is that to some

extent the effects will alter all the competing pathways in a similar manner, and although individual energies and rates will be imprecise, to a first approximation the qualitative trends and relative predictions should be robust.

### Kinetic & thermodynamic parameter estimation

Enthalpies of formation are evaluated from the CBS-QB3 results using Bond Additivity Correction (BAC) values available in CanTherm Version 2.1.7.<sup>53</sup> To calculate partition functions, the CanTherm software package was utilized with a frequency scale factor of 0.99 for CBS-QB3 and 0.967 for M06-2X/6-31G+(d,p). The results from potential energy scans  $V_i(\theta_i)$  are fit to a Fourier series in CanTherm and the resulting coefficients  $A_m$  and  $B_m$  in eqn (1) are found using the least squares method.

$$V_i(\theta_i) = \sum_{m=1}^M A_{m,i} \cos(m\theta_i) + B_{m,i} \sin(m\theta_i) \quad (1)$$

wherein  $V_i$  is potential energy change due to torsion  $i$ .  $A_{m,i}$  and  $B_{m,i}$  are fitting parameters and  $\theta_i$  is the angle of rotation of the torsion  $i$ . The potential values were then used in solving the 1D Schrodinger equation to finally combine the harmonic oscillator (HO) approximation with the hindered rotor contribution. Entropy calculations considered molecular symmetry. Conventional transition state theory was used for calculating rate coefficients for considered pathways, with Eckart tunneling corrections to improve estimated rate coefficients at HTL-relevant temperatures. Rate constants were then fit to the modified Arrhenius equation (eqn (2)) for each of the  $i^{\text{th}}$  reactions where  $k_i$  is the rate constant for each reaction,  $A_i$  is the pre-exponential factor,  $E_i$  is the activation energy,  $n$  is a modification factor to represent the changes more accurately with temperature, and  $T$  is the temperature in Kelvin.<sup>54</sup>

$$k_i = A_i T^n \exp\left(\frac{-E_i}{RT}\right) \quad (2)$$

### Kinetic modeling

Thirty-eight reactions consisting of forty-seven molecules were proposed to describe initial intermediate nitrogen reactions in hydrothermal liquefaction. Arrhenius parameters for each reaction were calculated as described above then combined with their respective first and second order rate expressions to form a system of forty-eight ordinary differential equations (eqn (3)). This system constituted the kinetic model, which was then integrated in MATLAB using ode15s given initial conditions corresponding to the fractional feed composition of the amino acid ( $M_1$ ), lipid ( $M_7$ ), and carbohydrate ( $M_{12}$ ,  $M_{18}$ ,  $M_{26}$ , or  $M_{35}$ ). Kinetics calculations were completed as a function of temperature and reaction time. As discussed later, initial compositions covered the ternary compositional space defined in Table 1. Rates were calculated at 300–1000 K. All simulations were integrated over 30 minutes, unless denoted otherwise, to be consistent with typical experimental HTL

timescales. Simulations did not consider secondary reactions to higher molecular weight polymers, chars or phase changes.

$$\frac{dc_j}{dt} = \sum_{i=1}^N \nu_{ij} \times r_i \quad (3)$$

$$r_i = k_i(T) \prod_{j=1}^M c_j^{-\nu_{ij}} \text{ for } \nu_{ij} < 0$$

where  $c_j$  is the concentration of species  $j$  of  $M = 47$  species;  $\nu_{ij}$  is the stoichiometric coefficient of species  $j$  in reaction  $r_i$  of  $N = 38$  reactions. Reaction rates were calculated with mass action kinetics based on the proposed mechanism using rate constants described in eqn (2), as summarized in Table S3.†

### Experimental methods

Hydrothermal liquefaction experiments were conducted in a 300 mL stainless-steel Parr reactor (Model 4561) fit with a magnetic stirrer consistent with previous studies.<sup>9,55</sup> For each experiment, 100 g of food waste slurry (15 wt% solids) was loaded into the reactor. The food waste slurry was prepared as previously described<sup>9,55</sup> and according to Army specifications using a mixture of applesauce, chicken, butter, green beans, rice, instant potatoes, and cheese. After loading, the reactor was sealed and purged three times with nitrogen to remove residual air before pressurization to  $65.5 \pm 5$  bar and heating to  $575 \pm 5$  K at approximately  $279 \text{ K min}^{-1}$  using an external heating jacket. After heating, the reactor pressure was  $200 \pm 5$  bar, sufficient to maintain water in its liquid state. The reaction temperature was maintained for 60 minutes, at which point the reaction was quenched by placing the reactor in an ice bath until the measured temperature reached  $310 \pm 2$  K. Quenching required less than 10 minutes. The biocrude/solid mixture was then separated from the aqueous phase *via* vacuum filtration before the solids and biocrude were isolated using acetone. The acetone was then evaporated using a rotary evaporator to obtain the final mass of biocrude. Each product phase was carefully massed to ensure closure of the mass balance, as described previously.<sup>9,55</sup> Deliberate safety precautions were made to handle the high pressure and high temperature reaction mixture. All experiments were conducted in a ventilated fume hood with a properly sized rupture disk (172 bar) vented to the hood. The reactor was pressure tested with nitrogen at ambient temperature to 69 bar prior to each run.

All runs were completed in triplicate, with yield measurements agreeing to within  $\pm 10\%$  when experiments were performed under identical conditions. Average values obtained from these experiments are presented here.

HTL biocrude was analyzed *via* GC-MS, to understand the molecular composition of the volatile fraction. Biocrude and aqueous samples were dissolved in toluene to a final concentration of  $125 \mu\text{g mL}^{-1}$  for positive-ion APPI Fourier transform ion cyclotron resonance mass spectrometry (FT-ICR MS). Dissolved samples were analyzed using a custom-built FT-ICR mass spectrometer,<sup>56</sup> equipped with a 22 cm room temperature bore 9.4 T superconducting solenoid magnet (Oxford

Instruments, Abingdon, U.K.) and a modular ICR data collection station (Predator).<sup>33</sup> Both techniques are described further in the ESI.† Further analysis was completed to close the mass balance for carbon, nitrogen, and oxygen. Total organic carbon (TOC) and total nitrogen (TN) analyses were completed on the aqueous phase using a TOC analyzer (Shimadzu Co. Kyoto, Japan). Elemental analysis of the biocrude and char phases was completed by Midwest Microlabs (Indianapolis, IN). The hydrogen and oxygen composition of the aqueous phase was taken to be the difference between the total feed oxygen content and the sum of the remaining products.

## Results and discussion

In this work, reaction pathways for the liquefaction of carbohydrate, protein, and lipid monomers are explored through an analysis of thermodynamic reaction equilibrium and kinetics. GC-MS analysis of biocrude from food waste HTL is used to gain an understanding of small biocrude-phase products. A density functional theory (DFT) model is used on proposed reaction schemes involving six primary pathways for the formation of HTL intermediates. Free energy and Arrhenius parameters are calculated and utilized in the development of a kinetic model to evaluate the rates at which these reactions occur. This analysis provides a baseline for understanding the feasibility of the proposed pathways *via* a discussion of the coupling reactions from the primary model products to the larger molecules seen in HTL biocrude. FT-ICR MS was employed to validate model predictions through comparisons between the carbon number and double bond equivalency of

computationally-predicted and experimentally-observed product molecules.

### Experimental analysis of volatile HTL products

To ascertain the role and molecular contributions of nitrogen during the HTL process, a food waste slurry consisting of 18% protein, 59% carbohydrate, and 22% lipid was heated to 575 K for 60 minutes at 200 bar. This reaction produced, on average, 14% biocrude, 25% solid, and 17% aqueous products on a mass basis. Resultant mass yields were used in conjunction with the elemental composition of each phase to close carbon, nitrogen, hydrogen, and oxygen mass balances within 10%. This analysis shows that the feed contains 3.8% nitrogen, of which, 13.2% is found in the biocrude. The nitrogen product fractionation for food waste HTL can be seen in Fig. 2, wherein nearly 50% of the nitrogen partitions to the aqueous phase, consistent with previous literature findings.<sup>20,57</sup> The gas phase was found to contain >98% CO<sub>2</sub>, consistent with prior work showing only trace amounts of gas-phase ammonia.<sup>58,59</sup> Gas-phase nitrogen is below detection limits, leading to it being lumped together with loss, resulting in 95% mass balance closure. Nearly 60% of the nitrogen can be found in the liquid products (biocrude and aqueous), which are assumed to be miscible at reaction conditions, but phase partitioned at ambient temperature. These two phases have the potential to undergo the same reactions before thermodynamic partitioning occurs upon quenching.

Further analysis utilizing GC-MS (Fig. S1, Table S1†) of the volatile portion of biocrude allows for molecular-level analysis of small molecules where 86% of the total peak area was identified as fatty acids. Fatty acids were confirmed as the most abundant product *via* GC × GC-HRT, further identifying

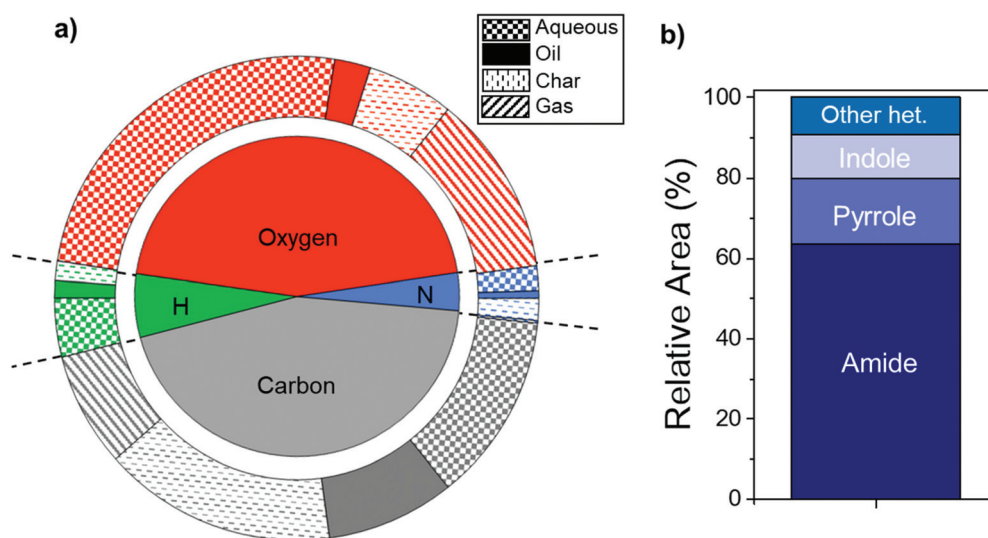


**Fig. 2** (a) Elemental analysis tracking the fate of carbon, hydrogen, oxygen, and nitrogen from food waste feedstock (inner circle) to HTL products (outer ring). HTL was performed at 575 K, 1 h residence time. (b) GC-MS peak area percentages for the total nitrogen identified in the oil phase, broken into prominent classes. Indoles, pyrroles, and other N heterocycles can be grouped together as the total nitrogen heterocycle content.

a suite of fatty acid amides corresponding to the same range of carbon chain lengths (Fig. S2†). The second most abundant class is nitrogen-containing compounds, of which 64% have been identified as amides (Fig. 2b). Further analysis of the chromatogram identifies a range of pyrroles, pyrrolidines, and indoles, all classes of nitrogen heterocycles, which accounted for the remaining 36% of the nitrogen compounds identified. Pyrroles account for nearly half of the identified heterocycles and indoles for an additional 30%. These compounds contain nitrogen locked in a ring structure, making them difficult to upgrade and remove. Their presence in HTL biocrude is of express interest in this work.

### Simulation of reaction intermediates

Due to the short-lived nature of the reactive small molecules and computational limitations, model species representative of the protein, carbohydrates, and lipid degradation products from food waste were chosen as feedstock molecules. Additional carbon atoms will serve to increase the hydrophobicity at room temperature and can play a role in increased steric hinderance that can affect experimental reaction rates. For this study, glycine was utilized as the model protein, butadiene as the model fatty acid, and four aldehydes (formaldehyde, glyoxal, furaldehyde, and glyceraldehyde) as model carbohydrates. Reaction chemistries commonly identified in literature were evaluated and compared including combination (condensation, cyclization, dehydration) and decomposition (hydrolysis, deamination, decarboxylation) reactions.

At HTL conditions, inorganic and small organic nitrogen molecules readily break down into amines at high temperatures in basic media through various deamination pathways.<sup>60</sup> Heterocycles, such as pyrroles and indoles, which are present in the side chain of amino acids proline, histidine, and tryptophan, lock their nitrogen in a stable aromatic ring structure which requires severe reaction conditions to break down. The Maillard reaction is a well-known heterocyclic reaction responsible for the browning of foods.<sup>61,62</sup> Maillard reactions occur between a carbonyl group on a reducing sugar and the amine group of a protein, and have been shown to proceed through pH-dependent pathways.<sup>63,64</sup> Specifically, retro-aldol reactions are more prominent at basic pH, producing more reactive C<sub>2</sub>–C<sub>5</sub> sugar fragments.<sup>63</sup> An additional reaction of importance is the Aza-Diels Alder (ADA) reaction, which has not received as much research attention as the well-known Diels–Alder reaction. ADA represents the cycloaddition of a diene and dienophile without an imine group.<sup>65,66</sup> This reaction is thought to occur *via* a single transition state without intermediates. Based on HTL literature and established chemical pathways, the final reaction scheme was reduced to those shown in Fig. 3.<sup>20,31,42,43,65,67–75</sup> Studied reactions are divided into six primary pathways denoted by their initial reactants, and all molecules are summarized in Table S2.†

Scheme 1 is the result of glycine decomposition in four potential competitive pathways including decarboxylation (1.5) and deamination (1.3). Schemes 2–4 involve the addition of increasingly oxygenated aldehydes (formaldehyde, furalde-

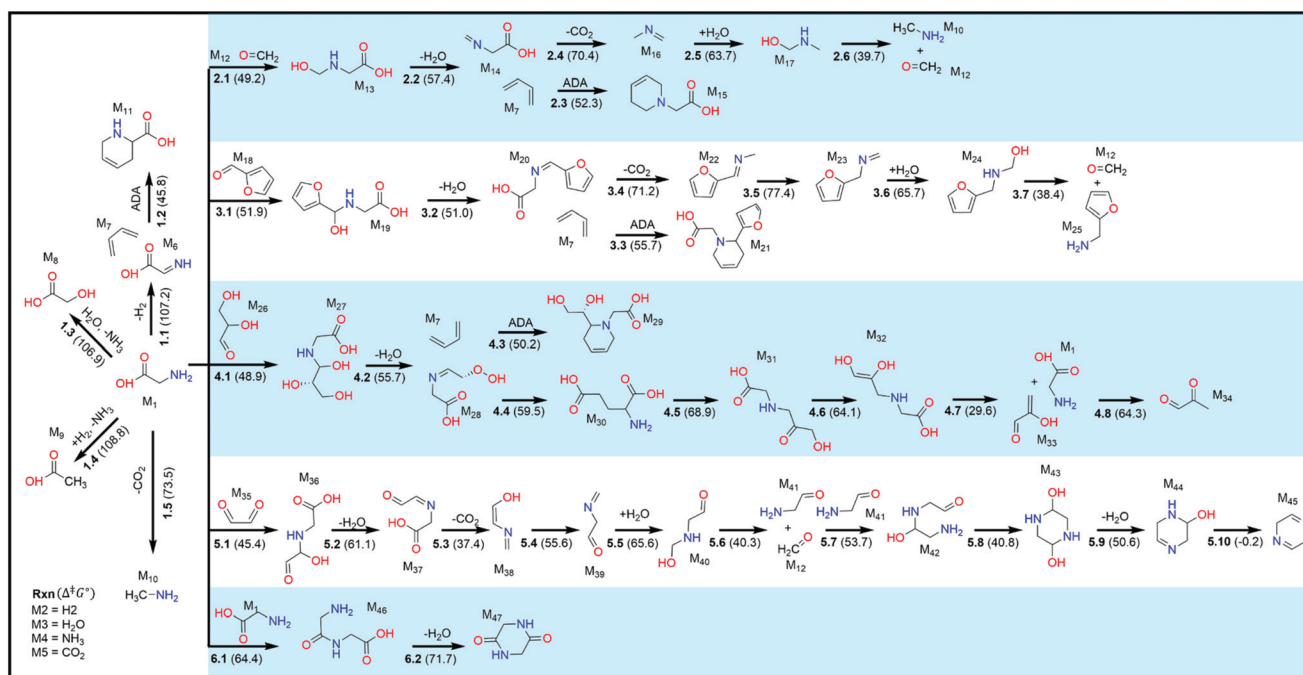


**Fig. 3** Overall reaction network divided into six primary reactions schemes. Scheme 1 shows four decomposition routes for the thermolysis of glycine. Schemes 2, 3, and 4 show the reactions of glycine with four different aldehydes (formaldehyde, glyoxal, furaldehyde, and glyceraldehyde) and showcase the competitive Aza Diels Alder (ADA) reaction to nitrogen heterocycle formation. Scheme 5 is a modified Maillard reaction and Scheme 6 showcases the self-combination route of two glycine molecules.  $\Delta^\ddagger G^\circ$  [=] kcal mol<sup>-1</sup>.

hyde, glyceraldehyde). Each of the aforementioned schemes include a pathway to the primary amine and a competitive reaction (2.3, 3.3, 4.3) resulting in nitrogen heterocycle formation through the ADA reaction mechanism. The remaining secondary reactions in these schemes do not result in heterocycle formation but include rearrangements, aminations, dehydration, and decomposition reactions. Scheme 5 represents a modified Maillard reaction for the formation of a nitrogen heterocycle. This is an important reaction to consider due to its prevalence in literature and as a dominant heterocycle formation mechanism. The Maillard reaction contains ten intermediates, making it the longest scheme with multiple kinetic barriers and free energy increases to overcome. The last scheme considered, (6) outlines the pathway for the combination of two glycine molecules through dehydration to form a nitrogen heterocycle.

Transition state theory is used to calculate the temperature-dependent reaction rates while accounting for tunneling effects and fit to a modified Arrhenius equation (eqn (2)) as reported in Table 2. The Eyring equation is then used to derive

**Table 2** Modified Arrhenius rate parameters (eqn (2)) calculated using the CBS-QB3 method. Calculated rate constant for all reactions at 600 K

Reaction	$A_i$	$n$	$E_i$ (kcal mol <sup>-1</sup> )	$k_i$ (600 K)	Class <sup>c</sup>
1.1 <sup>a</sup>	$2.4 \times 10^{-79}$	27.34	64.1	$1.0 \times 10^{-26}$	Degradation
1.2 <sup>b</sup>	$1.8 \times 10^{04}$	1.53	20.3	$1.3 \times 10^{01}$	ADA <sup>c</sup>
1.3 <sup>b</sup>	$4.0 \times 10^{01}$	3.04	85.7	$6.6 \times 10^{-22}$	Deamination <sup>c</sup>
1.4 <sup>b</sup>	$4.7 \times 10^{06}$	2.07	94.1	$1.3 \times 10^{-22}$	Deamination <sup>c</sup>
1.5 <sup>a</sup>	$1.1 \times 10^{-24}$	11.07	56.2	$2.0 \times 10^{-14}$	Decarboxylation <sup>c</sup>
2.1 <sup>b</sup>	$4.6 \times 10^{-05}$	4.29	21.2	$7.1 \times 10^{-01}$	Combination
2.2 <sup>a</sup>	$1.0 \times 10^{-06}$	5.71	48.6	$1.5 \times 10^{-08}$	Dehydration
2.3 <sup>b</sup>	$3.0 \times 10^{-01}$	2.69	22.6	$5.3 \times 10^{-02}$	ADA <sup>c</sup>
2.4 <sup>a</sup>	$4.6 \times 10^{-33}$	13.58	49.3	$2.6 \times 10^{-13}$	Decarboxylation <sup>c</sup>
2.5 <sup>b</sup>	$6.2 \times 10^{01}$	3.12	43.6	$3.8 \times 10^{-06}$	H <sub>2</sub> O Addition
2.6 <sup>a</sup>	$5.9 \times 10^{02}$	2.86	33.2	$4.4 \times 10^{-02}$	Degradation
3.1 <sup>b</sup>	$1.3 \times 10^{-06}$	4.65	22.4	$7.6 \times 10^{-02}$	Combination
3.2 <sup>a</sup>	$3.3 \times 10^{18}$	-1.57	54.0	$3.1 \times 10^{-06}$	Dehydration
3.3 <sup>b</sup>	$5.7 \times 10^{-01}$	2.32	23.9	$3.0 \times 10^{-03}$	ADA <sup>c</sup>
3.4 <sup>a</sup>	$1.3 \times 10^{-31}$	13.03	49.9	$1.3 \times 10^{-13}$	Decarboxylation <sup>c</sup>
3.5 <sup>a</sup>	$2.9 \times 10^{-07}$	5.86	68.3	$7.4 \times 10^{-16}$	Rearrangement
3.6 <sup>b</sup>	$3.8 \times 10^{-01}$	3.48	42.3	$6.9 \times 10^{-07}$	H <sub>2</sub> O Addition
3.7 <sup>a</sup>	$4.6 \times 10^{12}$	-0.06	36.8	$1.3 \times 10^{-01}$	Remove CH <sub>2</sub> O
4.1 <sup>b</sup>	$1.5 \times 10^{01}$	2.21	20.2	$9.0 \times 10^{-01}$	Combination
4.2 <sup>a</sup>	$8.0 \times 10^{08}$	0.91	51.2	$6.2 \times 10^{-08}$	Dehydration
4.3 <sup>b</sup>	$4.5 \times 10^{01}$	-0.67	25.5	$3.3 \times 10^{-01}$	ADA <sup>c</sup>
4.4 <sup>a</sup>	$5.7 \times 10^{-14}$	8.42	51.4	$2.6 \times 10^{-09}$	Rearrangement
4.5 <sup>a</sup>	$7.6 \times 10^{-01}$	3.43	58.9	$9.3 \times 10^{-13}$	Rearrangement
4.6 <sup>a</sup>	$3.2 \times 10^{-30}$	12.83	45.1	$5.3 \times 10^{-11}$	Rearrangement
4.7 <sup>a</sup>	$1.8 \times 10^{16}$	-1.13	29.7	$2.0 \times 10^{02}$	Degradation
4.8 <sup>a</sup>	$5.5 \times 10^{-47}$	18.11	39.5	$4.6 \times 10^{-11}$	Rearrangement
5.1 <sup>b</sup>	$7.7 \times 10^{-04}$	3.75	16.6	$1.8 \times 10^{01}$	Combination
5.2 <sup>a</sup>	$9.3 \times 10^{17}$	-1.31	64.6	$6.5 \times 10^{-10}$	Dehydration
5.3 <sup>a</sup>	$1.4 \times 10^{12}$	-0.25	32.9	$2.9 \times 10^{-01}$	Decarboxylation
5.4 <sup>a</sup>	$1.4 \times 10^{-29}$	12.66	37.0	$6.7 \times 10^{-08}$	H <sub>2</sub> O Addition
5.5 <sup>b</sup>	$4.0 \times 10^{-20}$	9.16	33.4	$7.9 \times 10^{-07}$	Decomposition
5.6 <sup>a</sup>	$3.6 \times 10^{13}$	-0.24	39.7	$2.7 \times 10^{-02}$	Addition
5.7 <sup>b</sup>	$5.7 \times 10^{-07}$	4.44	21.6	$1.7 \times 10^{-02}$	Rearrangement
5.8 <sup>a</sup>	$8.3 \times 10^{09}$	-0.15	31.0	$1.7 \times 10^{-02}$	Dehydration
5.9 <sup>a</sup>	$2.5 \times 10^{15}$	-0.35	54.2	$4.6 \times 10^{-06}$	Dehydration
5.10 <sup>a</sup>	$1.1 \times 10^{13}$	0.44	3.0	$1.5 \times 10^{13}$	Dehydration
6.1 <sup>b</sup>	$2.0 \times 10^{-01}$	2.87	35.5	$2.2 \times 10^{-06}$	Coupling
6.2 <sup>a</sup>	$1.7 \times 10^{06}$	1.23	62.3	$8.9 \times 10^{-14}$	Condensation <sup>c</sup>

<sup>a</sup> 1<sup>st</sup> order reaction with units  $A$  [=] s<sup>-1</sup>,  $k$  [=] s<sup>-1</sup>. <sup>b</sup> 2<sup>nd</sup> order reaction with units  $A$  [=] cm<sup>3</sup> mol<sup>-1</sup> s<sup>-1</sup>,  $k$  [=] cm<sup>3</sup> mol<sup>-1</sup> s<sup>-1</sup>. <sup>c</sup> Indicates primary reaction mechanism corresponding to colors in Fig. 4.

the Gibbs energy of activation ( $\Delta^\ddagger G^\circ$ ) at 600 K, as described in the ESI.† This strategy allows for the evaluation of the free energy change for the reaction, indicating the favorability of the reaction, as well the activation free energy, representing the  $\Delta G$  of the transition state. An exergonic decrease in free energy signifies the system releases energy spontaneously and is favorable in comparison to an endergonic increase in free energy where further energy inputs are required. Likewise, a high activation free energy signifies a slow reaction, and a low activation free energy signifies a faster reaction. Transition state activation free energy and free energy of reactants are shown on the free energy surfaces in Fig. 4 and tabulated in Table S3,† all evaluated at 600 K. Reaction schemes are colored based on the reaction step with the largest activation energy, except when the largest step is a rearrangement reaction. The  $\Delta^\ddagger G^\circ$  values at 600 K are also shown in parentheses next to the reaction numbers in Fig. 3 and are the activation barriers described in the following discussion.

In Scheme 1, the deamination and decarboxylation of glycine in reactions 1.4 and 1.5 are the most exergonic first-step reactions, however, reaction 1.4 has the highest activation barrier of the reaction network at 109 kcal mol<sup>-1</sup>. The decarboxylation in reaction 1.5 has the lowest barrier of the initial competitive steps in Scheme 1 at 74 kcal mol<sup>-1</sup>. Reaction 1.1 and 1.3 also boast high activation barriers, both at 107 kcal mol<sup>-1</sup>. Glycine decomposition through the deamination pathway (1.4), despite its activation energy, has been shown to occur at temperatures as low as 559 K, making this pathway the most probable first reaction step in Scheme 1.<sup>76</sup>

In Scheme 2, the formation of a nitrogen heterocycle through ADA is kinetically limited by reaction 2.2 in which the hemiaminal formed in the previous reaction undergoes dehydration to a Schiff base. This reversible reaction becomes increasingly exergonic (and hence spontaneous) as temperatures rise above about 400 K but has the highest barrier in Scheme 2 (57 kcal mol<sup>-1</sup>) and a rate strongly dependent on reaction temperature. The ADA reaction (2.3) occurs with a slightly lower energy barrier (52 kcal mol<sup>-1</sup>) than the competing reaction. Reaction 2.3 also has a lower energy barrier than the competing decarboxylation reaction, indicating heterocycle favorability. The same analysis holds true for Schemes 3 and 4, wherein ADA has a lower activation barrier than the competing reactions studied. The predicted nitrogen heterocycles from ADA are all substituted pyridines, wherein GC-MS analysis does not identify any pyridines but instead has a higher concentration of nitrogenated five-membered rings. This may be due to the presence of tryptophan in real food waste that is not considered in the model.

In Scheme 5, many of the reactions have energy barriers above 50 kcal mol<sup>-1</sup>. Reaction 5.2 of the Maillard reaction has a large activation energy at 61 kcal mol<sup>-1</sup> and reaction 5.5 has the largest energy barrier at 66 kcal mol<sup>-1</sup>. Reaction 5.2, the formation of a Schiff base, is reversible, but at typical HTL conditions the reverse rate is negligible, especially compared to the onward reaction 5.3, and has not been considered. The Strecker Degradation (SD) that occurs in the final stages of the

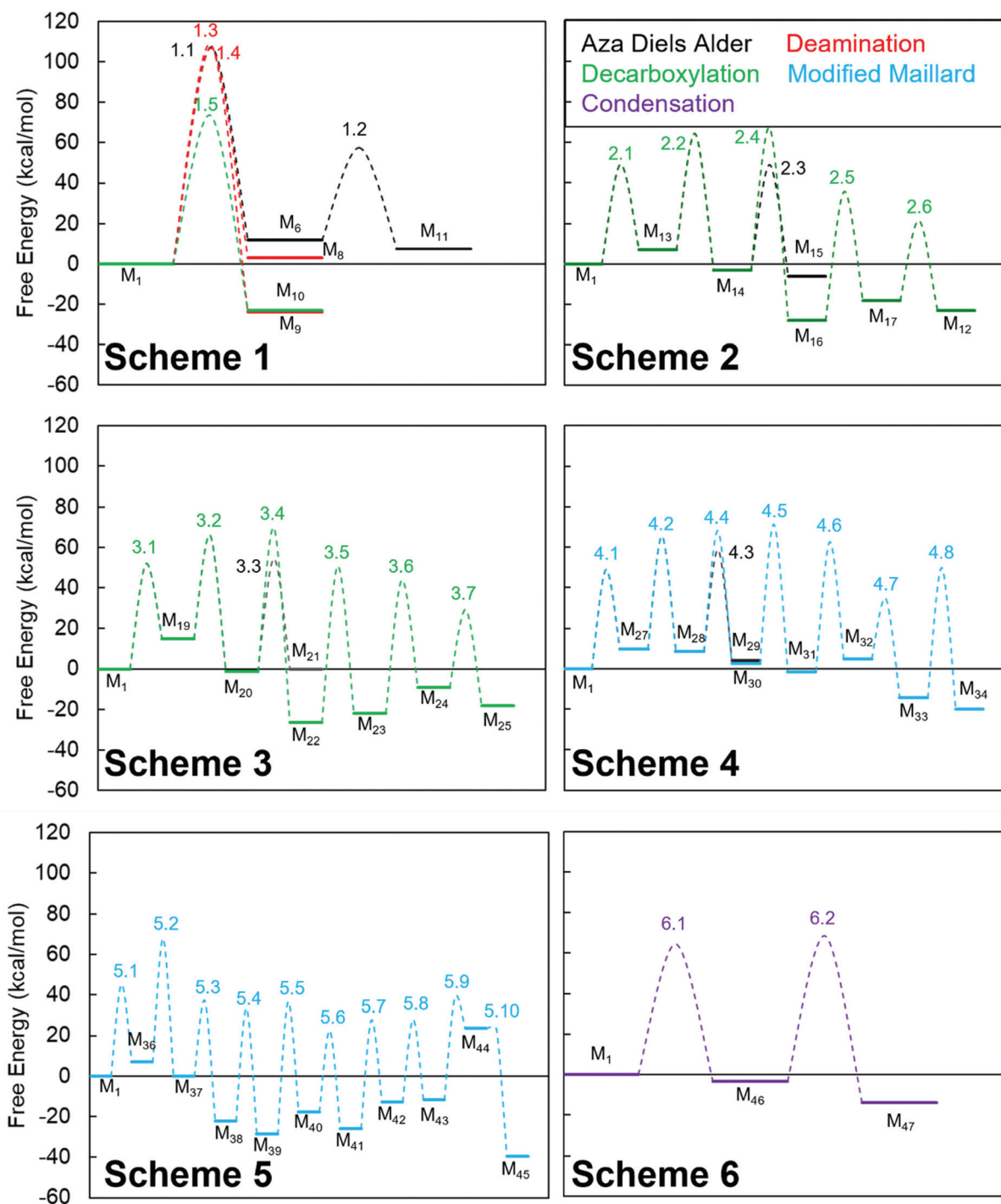


Fig. 4 Free energy diagram for all reaction pathways at 600 K. Reaction pathways are colored based on the reaction step with the largest activation energy, except when a rearrangement reaction had the highest activation energy.

pathway (5.2) as well as the dicarbonyl produced from the Amadori rearrangement (5.4) react with an amino acid (glycine) to produce a hemiaminal (5.7) *via* a mechanism with an energy barrier of 54 kcal mol<sup>-1</sup>, after the second rate-limiting step at 5.5. This reaction is the dehydration of a previously formed nitrogen heterocycle (1,2,3,6-tetrahydropyrazin-2-ol) to 2,5-dihydropyrazine. Reaction 5.8 is necessary for nitrogen het-

erocycle formation, followed by two dehydration rearrangements. Due to the large energy barrier of reaction 5.9, it is most likely that piperazine-2,5-diol (M<sub>43</sub>) will be the final product of this reaction scheme. Experimentally, only one pyrazine compound was identified with GC-MS constituting 2% of the nitrogen-containing compounds. Contrary to the model predicting alcohol-substituted pyrazine, the observed molecule

is methylated, potentially indicating the prevalence of tertiary dehydration reactions at longer residence times. On the other hand, the coupling of two glycine molecules in Scheme 6 *via* dehydration occurs with an energy barrier of 64 kcal mol<sup>-1</sup>, indicating the enhanced stability of glycyglycine (M<sub>46</sub>) and the potentially unfavorable dehydration to piperazine-2,5-dione (M<sub>47</sub>).

Another consideration, across all schemes, is the formation of gaseous byproducts. CO<sub>2</sub> is produced in reactions 1.5, 2.4, 3.4, and 5.3 while NH<sub>3</sub> can be found in reactions 1.3 and 1.4. All CO<sub>2</sub> formation reactions considered are thermodynamically favorable at 600 K, constituting a decrease in free energy, whereas only one of the two ammonia producing reactions is exergonic. Kinetically, all reactions forming CO<sub>2</sub> as a byproduct have lower activation energies than the two NH<sub>3</sub> reactions by at least 33 kcal mol<sup>-1</sup>. This finding is consistent with experimental results, where over 98% of the gaseous products are carbon dioxide, and only trace ammonia is detected.

The kinetic parameters summarized in Table 2 are used to construct a model to perform a reaction flux analysis and identify dominant chemical pathways during hydrothermal operation, particularly with the goal of revealing pathways by which the observed heterocyclic nitrogen molecules are produced. The model does not consider further polymerization reactions, solely predicting the behavior of the intermediates. Cross reactions, wherein products from one scheme can react

with reactants or products from another scheme, were also not considered.

The molecules considered in this reaction network are distributed into fourteen chemical classes (Table S2†) for ease of reporting the kinetic model. The first three classes denote the primary reactants: amino acid, diene, and aldehyde which together account for six of the forty-seven molecules examined. Additional chemical classes identified are as follows: amine, amide, hemiaminals, amino-aldehydes, alkanolamines, acids, Schiff base, gases, nitrogen heterocycles, and other. These classes will be referenced throughout the remainder of this study.

### Temperature dependence

Standard HTL reactions take place between 525–675 K, resulting in a range of potential dominant reactions. Reaction temperature has been shown to affect HTL mass yields and composition.<sup>34</sup> One variable often considered is the optimal reaction temperature. Operating below 525 K often results in high solids (char) formation and is traditionally coined hydrothermal carbonization. The model assumes and kinetics confirm that the monomeric species are stable at these reaction temperatures, and will not couple to form oligomers, bio-crude-soluble products, or char. This observation is consistent with the understanding that carbonization primarily progresses directly from concerted biopolymer rearrangements,

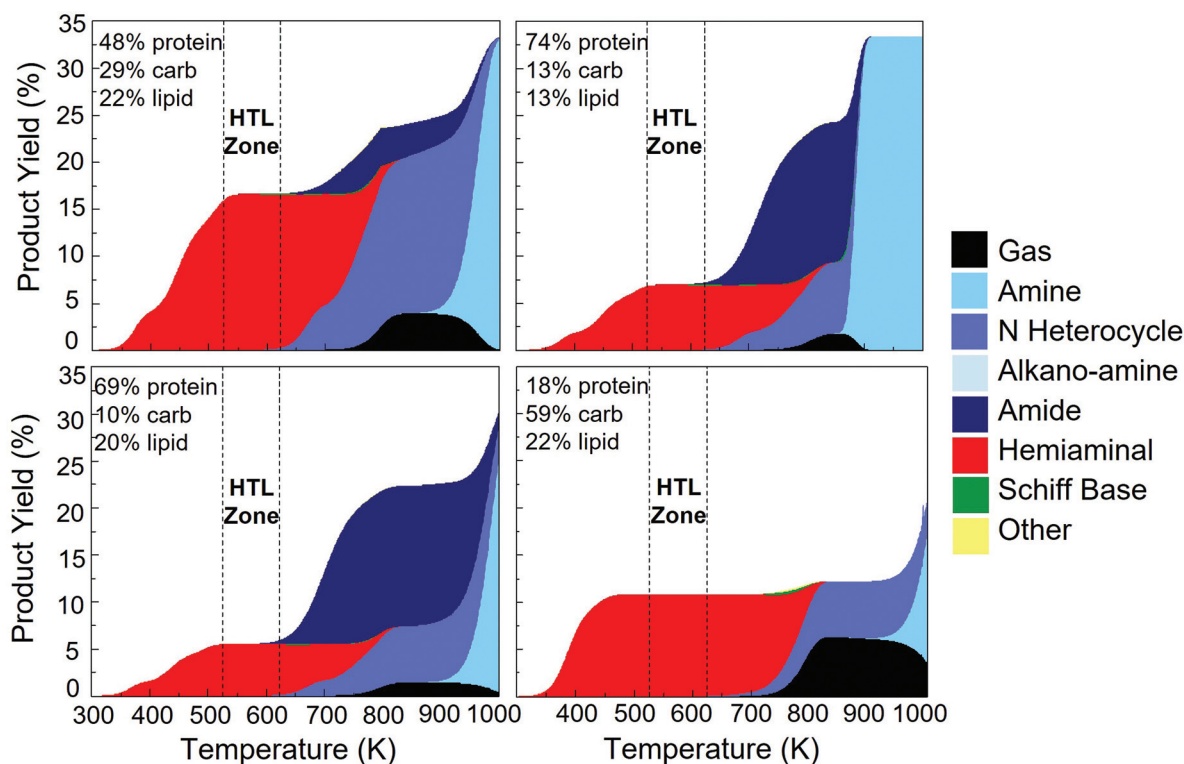


**Fig. 5** The effect of temperature on HTL intermediate product distributions for four surrogate feedstock compositions representative of food waste, and various algae streams. Shades of blue represent nitrogen containing classes identified in the GC-MS. Dashed lines indicate the temperature range for conventional HTL experiments. All models were completed at 30 min residence time for a range of 300–1000 K discretized to 1200 points.

not from the bottom-up approach whereby the biocrude is polymerized to char.<sup>77</sup> Hydrothermal liquefaction reactions, on the other hand, typically occur between 525–625 K to ensure complete breakdown of macromolecules and to limit low-temperature char formation. With this analysis, operating conditions can be fine-tuned to limit heterocycle production in the liquid products. Fig. 5 plots the effect of reaction temperature at 30 minutes for four real feedstock compositions taken from algae and food waste (Table S4†).<sup>9,16</sup> Carbohydrate concentration was divided evenly among the four possible reactant aldehydes. All kinetic simulations were assumed to be single phase in this study, and changes to physical or kinetic properties upon phase transition (oil/aqueous or supercritical) were not considered.

Low protein feeds (<50%) resulted in hemiaminals as the sole nitrogen intermediate product at HTL conditions (525–625 K). At these conditions, higher protein feeds also contain a small (<3%) fraction of amides that increases substantially with increasing temperature. When the majority of the feed is carbohydrates, no amide formation occurs at any of the explored temperatures, potentially due to the low concentration of glycine, inhibiting reaction 6.1 due to its high kinetic barrier compared to parallel steps in the competing schemes. There is no shortage of aldehydes to undergo Maillard and competing combination reactions. The model predicts an overwhelming majority of hemiaminals within traditional HTL temperature range, yet a small increase in temperature introduces unfavorable heterocycles as well as amide, gaseous, and amine products.

Despite predicting no appreciable formation of nitrogen heterocycles until 650 K, experimental findings from algae and food waste feeds have identified oil-phase heterocycles at 575 K. This is likely caused by a combination of unreactive side chains present in the native proteins and tertiary reactions whereby the intermediate products continue to react as they build up to larger biocrude molecules. Five of the twenty essential amino acids contain heterocyclic side chains and are likely present in food waste. In experiments performed between 550–590 K with algae, appreciable amounts of pyrroles, pyridines, indoles, diketopiperazines (DKPs), and imidazoles were identified in the biocrude.<sup>34,78</sup> Previously mentioned analysis with food waste HTL has also identified the presence of nitrogen heterocyclic compounds, despite reaction temperatures below 650 K.<sup>3</sup> The hemiaminals predicted by the model exhibit similar functionality to some of the observed heterocycles, including DKPs with the presence of nitrogen and double-bonded oxygen in the same molecule. Both have the potential to form from the interaction between amino acids and monosaccharides, often proceeding through a hemiaminal intermediate before the final cyclization step.<sup>79</sup> The experimentally observed heterocycles are larger (>C<sub>6</sub>) and likely result from secondary coupling reactions from the intermediate products predicted here. Additionally, the model predicts less than 2% of the products are heterocycles in the typical reaction temperature range. Notably, the vast majority of the nitrogen remains as unreacted glycine due to the initial energy

barriers to decomposition. The proposed model serves to understand dominant pathways and molecular functionality that are critical steppingstones towards further combination and cyclization interactions to produce the experimentally identified molecules.

### Feed composition effects

The composition of the feed can vary from 2–75% protein (Table 1), which can have a substantial effect on the prevalence of nitrogen reactions and resultant product distributions. Due to this large variance, Fig. 6 examines the effect of feedstock composition on the concentration of four nitrogen-containing product classes (amine, hemiaminal, amide, and nitrogen heterocycles). The kinetic model was run at 600 K for 30 minutes with starting feed compositions evenly distributed between the reactants in 1% discretization. Due to the exclusion of secondary coupling reactions of intermediate products, concentrations do not continue to change (within 1%) after this time for all simulations. Product classes were grouped so as to exclude the initial concentrations of amino acid, aldehyde, and diene. The resulting data was interpolated and presented as a heat map for the four heteroatom classes.

The amino acid, specifically glycine, is the sole reactant containing nitrogen in the model, leading to its concentration having the greatest effect on product distribution and yield. In the amine and amide classes, this trend is the clearest, where increased amino acid content directly increases resultant product concentration. The hemiaminal and nitrogen heterocycle classes, however, result in a more interesting trend that does not directly correlate with increasing amino acid concentration, indicating these molecules are the result of emergent monomeric interactions between macromolecule decomposition products. The hemiaminals (carbinolamines) are characterized by a hydroxyl and amine group attached to the same carbon, thereby opening additional pathways to formation including from aldehydes. Looking back to the reaction network, hemiaminals are products of the first reaction in Schemes 2, 3, and 4 (reactions 2.1, 3.1, and 4.1), which represents the addition of glycine with each of the starting aldehydes. It is for this reason that the highest concentration of hemiaminals occurs close to a 50:50 mixture of amino acid and aldehyde, continuing to decrease moving further away from the stoichiometric ratio.

While hemiaminal formation is relatively easy to explain, nitrogen heterocycle synthesis is more complicated. In the GC-MS analysis, HTL of food waste resulted in 36% of the volatile nitrogen species in the biocrude as heterocycles. Nitrogen heterocycles are formed in the reaction network in all schemes through a variety of pathways. Scheme 1 uses the Aza Diels Alder reaction to complete a cycloaddition of an imine (M<sub>6</sub>), formed from the dehydrogenation of the amino acid, with butadiene (M<sub>7</sub>). Schemes 2–4, however, react through the previously discussed synthesis of a hemiaminal (M<sub>13</sub>, M<sub>19</sub>, M<sub>27</sub>) which then undergoes dehydration to produce the reactive imine (M<sub>14</sub>, M<sub>20</sub>, M<sub>28</sub>). The Maillard reaction is responsible for nitrogen heterocycle formation in Scheme 5, wherein glycine

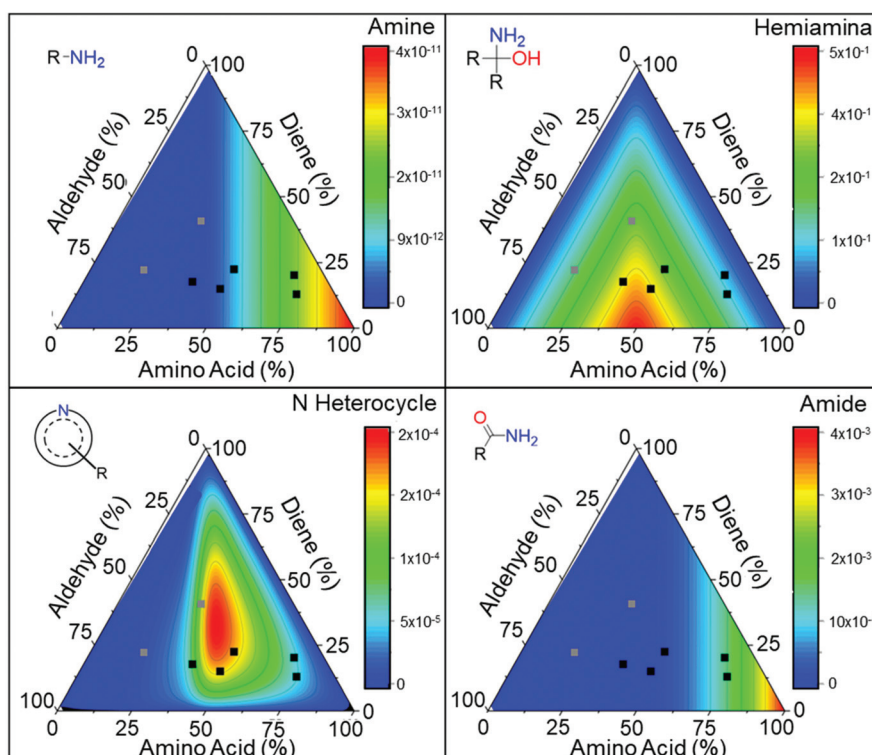


**Fig. 6** Ternary diagrams relating the product composition (color map) of four intermediate compound classes resulting from a particular starting composition defined on the ternary diagram. All data were taken interpolated from the kinetic model simulations at 600 K and 30-minute residence time. Black squares (■) represent known algae feedstock compositions and gray squares (□) are representative of food waste feedstocks where the aldehyde, amino acid and diene fractions are taken as surrogates for the carbohydrate, protein and fats, respectively. Color bar represents product concentration resulting from the kinetic model, [mol cm<sup>-3</sup>].

undergoes an addition reaction with glyoxal (M<sub>35</sub>, aldehyde) to form a hemiaminal (M<sub>36</sub>) before dehydration to produce an imine (M<sub>37</sub>). In Schemes 2–4, the same first three steps occur, with the addition of diene to promote nitrogen heterocycle formation. Scheme 5, on the other hand, does not include the addition of butadiene and instead allows for decarboxylation of the imine and subsequent hydrolysis and decomposition reactions leading to the formation of a Strecker aldehyde (M<sub>12</sub>) and a reductive amination product. In the last stage, condensation of the two amino-carbonyl compounds results in the formation of a nitrogen heterocycle (piperazinediol, M<sub>43</sub>) that can further dehydrate to pyrazine compounds (M<sub>44</sub>, M<sub>45</sub>). Lastly, Scheme 6 produces a nitrogen heterocycle through two subsequent dehydration and inter/intramolecular condensation reactions to form a diketopiperazine (M<sub>46</sub>).

In the kinetic analysis, Scheme 1 is not predicted to contribute substantially to the observed product distribution or heterocycle formation, likely due to the high activation barrier of reaction steps 1.1, 1.3, and 1.4 coupled with their slow rate constants on the order of  $10^{-50}$  s<sup>-1</sup> or cm<sup>3</sup> mol<sup>-1</sup> s<sup>-1</sup>. The rate constants of schemes 2–6 are comparable, indicating their similar reactivity and likelihood for these reactions to proceed. For this reason, Scheme 5 appears to contribute the most to heterocycle formation due to its sustained low activation bar-

riers, assuming the energy input is suitable to proceed past reaction 5.2 ( $\Delta^\ddagger G^\circ = 61.1$  kcal mol<sup>-1</sup>).

To further understand the effect of feedstock composition on nitrogen heterocycle formation, real feed compositions are referenced. In Fig. 6, the black squares are representative of various algae feedstocks while gray show food waste compositions, all highlighted in Table 1 and S3.‡ The comparatively low concentration of amines is primarily due to their role in the reaction scheme, wherein it is present as the reactant or as only one of the products of reaction 2.6. The lack of observed amines is indicative of their highly reactive nature in the reaction network and is consistent with GC-MS results which identified no primary amines in the product mixture (Fig. 2b).

Heterocycles are the sole class, of the four examined here, whose concentration depends on all three primary macromolecule contents. For this reason, the center of the high intensity area appears to occur near a stoichiometric mixture of all three reactants. All five algae compositions are within the bounds of increased heterocycle production. Food waste, on the other hand, often contains low protein and high carbohydrate content, indicative of the typical American diet. Of the two food waste feedstocks explored, one occurs in a region of moderate protein concentration while the other is in an area of low protein concentration. Recall, heterocycles are highly

undesired in biocrude, as it requires harsh hydrodenitrogenation (HDN) conditions to remove this nitrogen during upgrading. Elevated aromatic nitrogen has generally been observed in HTL oils from algal feeds, but lower amounts from food waste.<sup>80,81</sup> This is consistent with our model findings which show that sub-stoichiometric mixtures of protein results in lower heterocycle concentration. Cheng *et al.* has shown through FT-ICR MS that nitrogen heterocycles are present in both high and low-lipid algae biocrude in similar concentrations.<sup>34</sup> *N. salina*, a high-lipid algae, has shown to produce an oil high in alkyl substituted pyrroles and indoles, whereas *G. sulphuraria* biocrudes show higher degrees of alkylation with larger double-bond equivalency (DBE) range.<sup>34</sup> Low-lipid food waste, on the other hand, results in indoles as the primary heterocycle-still with an overall concentration less than 1%. This is most likely due to the presence of tryptophan as a common amino acid in chicken. Overall, the feed composition can be shown to be an important factor in determining the HTL product distribution.

### Closing the gap between small and large molecules

Making the connection back to experimental results, Fig. 7 showcases the observed trends between all nitrogen-containing heteroatom classes for both the biocrude and aqueous phases.

Positive ion APPI FT-ICR MS was utilized to probe the molecular space, revealing similarities in the carbon number and DBE relationship for both liquid phases (biocrude and aqueous) across heteroatom classes. DBE provides insight into chemical makeup by capturing the degree of unsaturation resulting from double bonds or rings, as is typically resultant from molecular condensations. All four nitrogen classes contain biocrude molecules with a DBE greater than five, indicating the presence of at least one ring structure. It can also be seen that with increasing nitrogen number, the lower DBE limit increases, indicating further formation of heterocycles, most likely *via* dimerization pathways. Tryptophan, with an indole side chain, has the potential to undergo the Maillard reaction to produce a molecule with two nitrogen and a DBE > 10, consistent with identified molecules in the N<sub>2</sub>O<sub>x</sub> heteroatom class. Dimerization of this molecule then results in a compound with DBE > 20, >C<sub>30</sub> and four nitrogen, also consistent with Fig. 7. Notably, over 70% of all observed nitrogen-containing compounds had <C<sub>40</sub>, suggesting that chain growth may be limited based on the availability of reactive amines and molecules larger than C<sub>50</sub> begin to partition to solid products.

Further comparisons of this data to macromolecular trends can be found in Fig. S3,† wherein the regions of high abundance are consistent with the polymerization of common

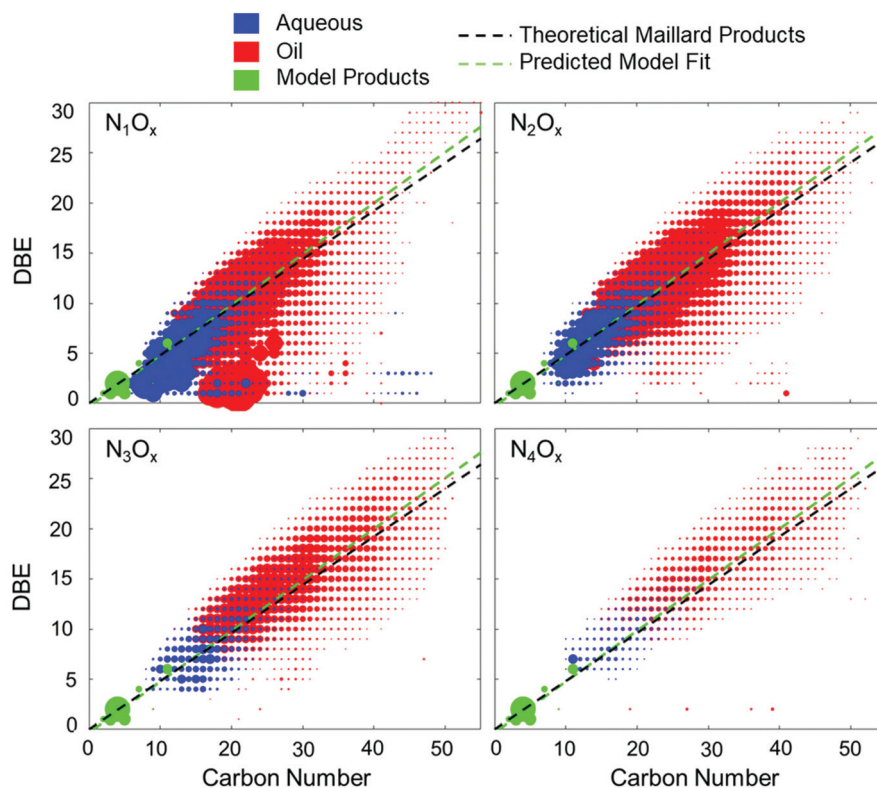


**Fig. 7** Double bond equivalency (DBE) versus carbon number for four nitrogen-containing heteroatom classes in the biocrude oil (red) and aqueous (blue) phases on food waste HTL at 575 K for 30 minutes. The green dots represented the products from the kinetic model (18% glycine, 22% diene, and 59% aldehyde split evenly between the four starting aldehydes). Model feedstock concentration was chosen to match that of the food waste HTL experiments. Experimental data points are sized by relative abundance and model points by relative concentration. The black dashed line represents the average trend for Maillard reaction products where the green line is the weighted average fit observed for products in the kinetic model.

carbohydrates and fatty acids. A compelling trend emerges from this data, whereby a strong linear relationship is observed across product classes. To better understand this trend, a range of chemistries were analyzed, starting with the Maillard reaction. By considering the chemistry that occurs during the Maillard reaction, it is noted that an amine condenses with a sugar molecule to form an *N*-substituted glycosylamine which undergoes Amadori rearrangement (5.4) to produce an Amadori rearrangement product (ARP). This is followed by a dehydration to produce furfurals and reductones, based on pH. Additionally, sugar fragmentation and Strecker degradation occur nearly simultaneously alongside the dehydration. During Strecker degradation, amino acids are oxidized in the presence of dicarbonyl compounds to produce CO<sub>2</sub>, aldehydes, and amino-ketones. The resultant aldehydes react with each other through aldol condensation in the final stage of the Maillard reaction. Finally, aldehydes react with amines through condensation and cyclization reactions to produce nitrogen heterocycles, including pyrroles, pyridines, and pyrazines. The Maillard reaction nets the loss of a carbon dioxide and three water molecules, with the addition of three R-NH<sub>2</sub> groups, effectively increasing the DBE by one (ring formation) and increasing the net carbon number by two, on average (DBE = 0.5 × C). To better approximate this trend, chemistries from literature were examined<sup>34,49,82</sup> by quantifying the change in DBE upon completion of the Maillard reaction as [(DBE)<sub>products</sub> - (DBE)<sub>reactants</sub>]/[(C)<sub>products</sub> - (C)<sub>reactants</sub>]; after doing this, the average relationship was updated as DBE = 0.48 × C, as plotted in Fig. 7 as a black dashed line. Previous work has identified the importance of the Maillard reaction in biocrude formation from model sugars and amino acids, citing the formation of pyrazines as well as increased production of aromatic amines and amides.<sup>49</sup>

A similar analysis was performed using the reaction chemistry examined in this work. Reaction pathways were weighted by product abundance and correlated to DBE to reveal a trend, DBE = 0.51 × C, with the corresponding fit plotted in green in Fig. 7. For comparison with experimentally observed products, the relationship is extrapolated to larger carbon numbers as the expectation is that the intermediates will couple to form the larger products in secondary reactions. Notably, this relationship holds true as the dominant trend from all three data sets: the monomeric reactions (kinetic model), the final aqueous, and the final oil products, suggesting that the Maillard reactions are a dominant coupling pathway. Furthermore, the trend underscores that for every two carbons, one DBE is introduced, suggesting that other pathways may also be involved, such as aldol condensation or cycloaddition. As can be seen in Fig. 7, the resultant model products correlate well with Maillard reaction products, consistent with the high degree of aromaticity observed in GC-MS. The trend also agrees with the identified pathways from the proposed intermediates to the highly aromatic compounds identified, indicative of aqueous phase molecules having a lower carbon number and DBE than oil molecules, with considerable overlap in their ranges. This suggests a common pathway for

the formation of biocrude and water-soluble molecules, and is consistent with the understanding that at reaction temperatures, the two phases are miscible and are only phase separated and partitioned upon cooling.<sup>9</sup> The FT-ICR MS findings show that polymerization is scale-independent where the ring structure and intra-chain unsaturations are maintained across small molecules in the aqueous and larger organics in the oil. Furthermore, the trend suggests a high degree of saturation, as in the monomeric species glycine, tetrahydropyridine, and *N*-methylmethanimine captured by this kinetic model. This serves as valuable insight into the validity of the model in accurately predicting key HTL intermediate product distributions.

To assess model robustness, a sensitivity analysis was performed to measure the effect of a 1% perturbation in rate constants on individual product yields. Fig. S4† reports these results, indicating the overall sensitivity of the competitive reactions 2.1, 3.1, 4.1, and 5.1 on overall product distribution and yields. The analysis highlights the competitiveness of the initial amine-oxygenate reactions and suggests that no single aldehyde functionality is solely responsible for the coupling reactions. Further discussion can be found in the ESI.†

Water also plays an integral role in the hydrothermal processing and chemical transformations examined in this study. In addition to being a reactant or product in 10 of the 38 reaction pathways examined, its ability to solvate the reaction species can play a potentially significant role in the reaction energetics and kinetics. The sensitivity analysis (Fig. S4†) confirms that water is in excess in the system and its final amount does not depend on the reaction rates ( $\sigma_{ij} = 0$  for all instances of *i* = water). Future work should attempt to resolve the specific role of water as a solvent in these key reaction pathways. In this study, all activity coefficients are assumed to be unity, indicating that non-ideal solvent interactions have been neglected. It has been shown that under supercritical conditions (675 K, 275 bar) the activity coefficient of water decreases to 0.5, thereby reducing the corresponding reaction rates by a factor of two.<sup>83</sup> While typical HTL reaction conditions are nearly 375 K and 75 bar below the explored supercritical conditions, the activity of water at these conditions remains relevant in improving the accuracy of the model.

The model pathways presented in this work are representative of elementary reactions that occur in the condensed phase chemistry during food waste HTL. As revealed by FT-ICR-MS, however, tens of thousands of unique species are detected across a wide molecular weight distributions ranging from light oxygenates to non-volatile hydrochars. Future work should (1) continue to explore elementary pathways with a larger breadth of functionality and sizes, (2) introduce solvent interactions to improve computational energetic calculation accuracy in the hydrothermal environment, and (3) consider the transient environmental changes in reaction environment due to primary (biopolymer degradation) and tertiary (polymerization) reactions.

## Conclusions

Experimental analysis of food waste HTL products has revealed the presence of organic nitrogen in the form of fatty amides, indoles, and amines. Particularly notable is the prevalence of nitrogen-containing heterocyclic aromatics, the removal of which by conventional hydrodenitrogenation is difficult but necessary to hit fuel quality standards and avoid NO<sub>x</sub> emissions. A detailed kinetic mechanism was proposed using model compounds representative of typical HTL feedstock monomers; subsequent DFT calculations and kinetic models were used to evaluate likely reaction pathways. The analysis revealed the Maillard reaction as a likely source of nitrogen heterocycle formation at HTL reaction conditions. FT-ICR MS characterization and analysis further supported this conclusion, revealing strong correlations between theoretical Maillard reaction products, experimentally measured HTL reaction products, and the model-predicted products.

These analyses serve to illuminate dominant chemistries and kinetic pathways by examining the activity of the highly reactive short chain intermediates that typically react on the order of seconds in HTL reactors. Substantial energetic barriers were shown to exist in deamination and cyclization reactions, whereas condensation and ADA pathways experienced relatively low activation barriers, due to the relative stability of the transition states. This led to nitrogen heterocycles and gaseous nitrogen only being observed at higher temperatures; hemiaminals are the dominant product at lower temperatures. Strong compositional effects were observed in the formation of nitrogen heterocycles, which required stoichiometric amounts of amine, aldehyde, and diene. Sub-stoichiometric amounts of diene promoted production of hemiaminal and amide products, which is consistent with known hydrothermal products resulting from low lipid feedstocks. The predicted model trends correlated well with the experimentally observed product distributions from food waste HTL, with the FT-ICR MS showing final liquid products—dimer- and trimerization of amino acids, carbohydrate hydrolysis products, and fats—consistent with the Maillard reactions observed in the kinetic model. Ultimately, imines and aldehydes have been shown to be key classes in the proposed model, further showcasing its importance and accuracy in predicting HTL nitrogen intermediates. Future model expansions should consider the secondary reactions between the intermediates toward the formation of larger final products and the inclusion of solvent effects. Based on this work, the thermal barriers to deamination are revealed to be substantial kinetic limitations, so catalytic promotion of those pathways may be necessary to overcome large activation energetics.

## Conflicts of interest

There are no conflicts to declare.

## Acknowledgements

The authors would like to thank Jeffrey R. Page for his helpful discussions and modeling assistance and Dr Geoffrey A. Tompsett for his insight and support. We also acknowledge the Department of Energy Bioenergy Technology Office (DE-EE0008513) for funding. HOL was partially supported for this work by the National Science Foundation GRF Program under award number 2038257. A portion of this work was performed at the National High Magnetic Field Laboratory, which is supported by the National Science Foundation Division of Materials Research and Division of Chemistry through Cooperative Agreement No. DMR-1644779 and the State of Florida.

## References

- 1 W.-T. Chen, M. A. Haque, T. Lu, A. Aierzhati and G. Reimonn, A perspective on hydrothermal processing of sewage sludge, *Curr. Opin. Environ. Sci. Health*, 2020, **14**, 63–73.
- 2 D. C. Elliott, P. Biller, A. B. Ross, A. J. Schmidt and S. B. Jones, Hydrothermal liquefaction of biomass: Developments from batch to continuous process, *Bioresour. Technol.*, 2015, **178**, 147–156.
- 3 A. R. K. Gollakota, N. Kishore and S. Gu, A review on hydrothermal liquefaction of biomass, *Renewable Sustainable Energy Rev.*, 2018, **81**, 1378–1392.
- 4 Y. Guo, W. Song, J. Lu, Q. Ma, D. Xu and S. Wang, Hydrothermal liquefaction of Cyanophyta: Evaluation of potential bio-crude oil production and component analysis, *Algal Res.*, 2015, **11**, 242–247.
- 5 H.-S. Hu, Y.-L. Wu and M.-D. Yang, Fractionation of bio-oil produced from hydrothermal liquefaction of microalgae by liquid-liquid extraction, *Biomass Bioenergy*, 2018, **108**, 487–500.
- 6 N. Neveux, A. K. Yuen, C. Jazrawi, M. Magnusson, B. S. Haynes, A. F. Masters, A. Montoya, N. A. Paul, T. Maschmeyer and R. de Nys, Biocrude yield and productivity from the hydrothermal liquefaction of marine and freshwater green macroalgae. (1873–2976 (Electronic)).
- 7 J. S. Rowbotham, P. W. Dyer, H. C. Greenwell and M. K. Theodorou, Thermochemical processing of macroalgae: a late bloomer in the development of third-generation biofuels?, *Biofuels*, 2012, **3**(4), 441–461.
- 8 J. D. Sheehan and P. E. Savage, Modeling the effects of microalga biochemical content on the kinetics and bio-crude yields from hydrothermal liquefaction, *Bioresour. Technol.*, 2017, **239**, 144–150.
- 9 F. Cheng, G. A. Tompsett, C. M. Murphy, A. R. Maag, N. Carabillo, M. Bailey, J. J. Hemingway, C. I. Romo, A. D. Paulsen, P. E. Yelvington and M. T. Timko, Synergistic Effects of Inexpensive Mixed Metal Oxides for Catalytic Hydrothermal Liquefaction of Food Wastes, *ACS Sustainable Chem. Eng.*, 2020, **8**(17), 6877–6886.

- 10 L. J. Snowden-Swan, Y. Zhu, S. B. Jones, D. C. Elliot, A. J. Schmidt, R. T. Hallen, J. M. Billing, T. R. Hart, S. P. Fox and G. D. Maupin, Hydrothermal Liquefaction and Upgrading of Municipal Wastewater Treatment Plant Sludge: A Preliminary Techno-Economic Analysis, *Energy*, 2016, PNNL-25464.
- 11 A. R. Maag, A. D. Paulsen, T. J. Amundsen, P. E. Yelvington, G. A. Tompsett and M. T. Timko, Catalytic Hydrothermal Liquefaction of Food Waste Using CeZrOx, *Energies*, 2018, **11**(3), 564.
- 12 EPA, U. S. U.S. Food Waste Statistics.
- 13 EPA, U. S. U.S Waste Fact Sheet.
- 14 EPA, U. S. Clean Cities Alternative Fuel Price Report.
- 15 A. Badgett, E. Newes and A. Milbrandt, Economic analysis of wet waste-to-energy resources in the United States, *Energy*, 2019, **176**, 224–234.
- 16 R. Shakya, S. Adhikari, R. Mahadevan, S. R. Shanmugam, H. Nam, E. B. Hassan and T. A. Dempster, Influence of biochemical composition during hydrothermal liquefaction of algae on product yields and fuel properties, *Bioresour. Technol.*, 2017, **243**, 1112–1120.
- 17 K. Paritosh, S. K. Kushwaha, M. Yadav, N. Pareek, A. Chawade and V. Vivekanand, Food Waste to Energy: An Overview of Sustainable Approaches for Food Waste Management and Nutrient Recycling, *BioMed Res. Int.*, 2017, **2017**, 2370927.
- 18 H. Li, Z. Liu, Y. Zhang, B. Li, H. Lu, N. Duan, M. Liu, Z. Zhu and B. Si, Conversion efficiency and oil quality of low-lipid high-protein and high-lipid low-protein microalgae via hydrothermal liquefaction, *Bioresour. Technol.*, 2014, **154**, 322–329.
- 19 A. Quinkenstein, D. Pape, D. Freese, B. U. Schneider and R. F. Hüttel, Biomass, Carbon and Nitrogen Distribution in Living Woody Plant Parts of Robinia pseudoacacia L. Growing on Reclamation Sites in the Mining Region of Lower Lusatia (Northeast Germany), *Int. J. For. Res.*, 2012, **2012**, 891798.
- 20 J. Lu, J. Zhang, Z. Zhu, Y. Zhang, Y. Zhao, R. Li, J. Watson, B. Li and Z. Liu, Simultaneous production of biocrude oil and recovery of nutrients and metals from human feces via hydrothermal liquefaction, *Energy Convers. Manage.*, 2017, **134**, 340–346.
- 21 W. Li, Y. Zhao, C. Yao, J. Lu, R. Li and Y. Wu, Migration and transformation of nitrogen during hydrothermal liquefaction of penicillin sludge, *J. Supercrit. Fluids*, 2020, **157**, 104714.
- 22 F. Wang, Y. Tian, C.-C. Zhang, Y.-P. Xu and P.-G. Duan, Hydrotreatment of bio-oil distillates produced from pyrolysis and hydrothermal liquefaction of duckweed: A comparison study, *Sci. Total Environ.*, 2018, **636**, 953–962.
- 23 T. Wang, Y. Zhai, Y. Zhu, C. Peng, B. Xu, T. Wang, C. Li and G. Zeng, Influence of temperature on nitrogen fate during hydrothermal carbonization of food waste, *Bioresour. Technol.*, 2018, **247**, 182–189.
- 24 C. U. Jensen, L. A. Rosendahl and G. Olofsson, Impact of nitrogenous alkaline agent on continuous HTL of lignocellulosic biomass and biocrude upgrading, *Fuel Process. Technol.*, 2017, **159**, 376–385.
- 25 E. M. Anderson, M. L. Stone, R. Katahira, M. Reed, W. Muchero, K. J. Ramirez, G. T. Beckham and Y. Román-Leshkov, Differences in S/G ratio in natural poplar variants do not predict catalytic depolymerization monomer yields, *Nat. Commun.*, 2019, **10**(1), 2033.
- 26 D. G. Brandner, J. S. Kruger, N. E. Thornburg, G. G. Facas, J. K. Kenny, R. J. Dreiling, A. R. C. Morais, T. Renders, N. S. Cleveland, R. M. Happs, R. Katahira, T. B. Vinzant, D. G. Wilcox, Y. Román-Leshkov and G. T. Beckham, Flow-through solvolysis enables production of native-like lignin from biomass, *Green Chem.*, 2021, **23**(15), 5437–5441.
- 27 M. S. Mettler, S. H. Mushrif, A. D. Paulsen, A. D. Javadekar, D. G. Vlachos and P. J. Dauenhauer, Revealing pyrolysis chemistry for biofuels production: Conversion of cellulose to furans and small oxygenates, *Energy Environ. Sci.*, 2012, **5**(1), 5414–5424.
- 28 P. Duan and P. E. Savage, Hydrothermal Liquefaction of a Microalga with Heterogeneous Catalysts, *Ind. Eng. Chem. Res.*, 2011, **50**(1), 52–61.
- 29 A. Gollakota and P. E. Savage, Fast and Isothermal Hydrothermal Liquefaction of Polysaccharide Feedstocks, *ACS Sustainable Chem. Eng.*, 2020, **8**(9), 3762–3772.
- 30 L. Leng and W. Zhou, Chemical compositions and wastewater properties of aqueous phase (wastewater) produced from the hydrothermal treatment of wet biomass: A review, *Energy Sources, Part A*, 2018, **40**(22), 2648–2659.
- 31 Y. Bareha, R. Girault, S. Guezal, J. Chaker and A. Trémier, Modeling the fate of organic nitrogen during anaerobic digestion: Development of a bioaccessibility based ADM1, *Water Res.*, 2019, **154**, 298–315.
- 32 R. Obeid, D. M. Lewis, N. Smith, T. Hall and P. van Eyk, Reaction kinetics and characterisation of species in renewable crude from hydrothermal liquefaction of monomers to represent organic fractions of biomass feedstocks, *Chem. Eng. J.*, 2020, **389**, 124397.
- 33 G. T. Blakney, C. L. Hendrickson and A. G. Marshall, Predator data station: A fast data acquisition system for advanced FT-ICR MS experiments, *Int. J. Mass Spectrom.*, 2011, **306**(2), 246–252.
- 34 F. Cheng, Z. Cui, L. Chen, J. Jarvis, N. Paz, T. Schaub, N. Nirmalakhandan and C. E. Brewer, Hydrothermal liquefaction of high- and low-lipid algae: Bio-crude oil chemistry, *Appl. Energy*, 2017, **206**, 278–292.
- 35 J. M. Jarvis, J. M. Billing, Y. E. Corilo, A. J. Schmidt, R. T. Hallen and T. M. Schaub, FT-ICR, MS analysis of blended pine-microalgae feedstock HTL biocrudes, *Fuel*, 2018, **216**, 341–348.
- 36 C. Torri, D. López Barreiro, R. Conti, D. Fabbri and W. Brillman, Fast Procedure for the Analysis of Hydrothermal Liquefaction Biocrude with Stepwise Py-GC-MS and Data Interpretation Assisted by Means of Non-negative Matrix Factorization, *Energy Fuels*, 2016, **30**(2), 1135–1144.

- 37 J. M. Jarvis, J. M. Billing, R. T. Hallen, A. J. Schmidt and T. M. Schaub, Hydrothermal Liquefaction Biocrude Compositions Compared to Petroleum Crude and Shale Oil, *Energy Fuels*, 2017, **31**(3), 2896–2906.
- 38 F. A. Fernandez-Lima, C. Becker, A. M. McKenna, R. P. Rodgers, A. G. Marshall and D. H. Russell, Petroleum Crude Oil Characterization by IMS-MS and FTICR MS, *Anal. Chem.*, 2009, **81**(24), 9941–9947.
- 39 S. Kim, R. P. Rodgers, G. T. Blakney, C. L. Hendrickson and A. G. Marshall, Automated electrospray ionization FT-ICR mass spectrometry for petroleum analysis, *J. Am. Soc. Mass Spectrom.*, 2009, **20**(2), 263–268.
- 40 M. Li, D. Cheng, X. Pan, L. Dou, D. Hou, Q. Shi, Z. Wen, Y. Tang, S. Achal, M. Milovic and L. Tremblay, Characterization of petroleum acids using combined FT-IR, FT-ICR-MS and GC-MS: Implications for the origin of high acidity oils in the Muglad Basin, Sudan, *Org. Geochem.*, 2010, **41**(9), 959–965.
- 41 S. Du, J. A. Valla and G. M. Bollas, Characteristics and origin of char and coke from fast and slow, catalytic and thermal pyrolysis of biomass and relevant model compounds, *Green Chem.*, 2013, **15**(11), 3214–3229.
- 42 M. Déniel, G. Haarlemmer, A. Roubaud, E. Weiss-Hortala and J. Fages, Hydrothermal liquefaction of blackcurrant pomace and model molecules: understanding of reaction mechanisms, *Sustainable Energy Fuels*, 2017, **1**(3), 555–582.
- 43 G. Candiano, G. M. Ghiggeri, G. Delfino, C. Quierolo, C. Cuniberti, E. Gianazza and P. G. Righetti, Reaction of lysine with aldoses, *Carbohydr. Res.*, 1985, **145**(1), 99–112.
- 44 T. Hayashi and M. Namiki, Role of Sugar Fragmentation in an Early Stage Browning of Amino-carbonyl Reaction of Sugar with Amino Acid, *Agric. Biol. Chem.*, 1986, **50**(8), 1965–1970.
- 45 C. Gai, Y. Zhang, W.-T. Chen, P. Zhang and Y. Dong, An investigation of reaction pathways of hydrothermal liquefaction using *Chlorella pyrenoidosa* and *Spirulina platensis*, *Energy Convers. Manage.*, 2015, **96**, 330–339.
- 46 D. López Barreiro, M. Beck, U. Hornung, F. Ronsse, A. Kruse and W. Prins, Suitability of hydrothermal liquefaction as a conversion route to produce biofuels from macroalgae, *Algal Res.*, 2015, **11**, 234–241.
- 47 W. Yang, X. Li, Z. Li, C. Tong and L. Feng, Understanding low-lipid algae hydrothermal liquefaction characteristics and pathways through hydrothermal liquefaction of algal major components: Crude polysaccharides, crude proteins and their binary mixtures, *Bioresour. Technol.*, 2015, **196**, 99–108.
- 48 B. Zhang, Q. Lin, Q. Zhang, K. Wu, W. Pu, M. Yang and Y. Wu, Catalytic hydrothermal liquefaction of *Euglena* sp. microalgae over zeolite catalysts for the production of bio-oil, *RSC Adv.*, 2017, **7**(15), 8944–8951.
- 49 C. Zhang, X. Tang, L. Sheng and X. Yang, Enhancing the performance of Co-hydrothermal liquefaction for mixed algae strains by the Maillard reaction, *Green Chem.*, 2016, **18**(8), 2542–2553.
- 50 B. L. Slakman and R. H. West, Kinetic solvent effects in organic reactions, *J. Phys. Org. Chem.*, 2019, **32**(3), e3904.
- 51 R. Bini, C. Chiappe, V. L. Mestre, C. S. Pomelli and T. Welton, A rationalization of the solvent effect on the Diels–Alder reaction in ionic liquids using multiparameter linear solvation energy relationships, *Org. Biomol. Chem.*, 2008, **6**(14), 2522–2529.
- 52 W. M. Baisier and T. P. Labuza, Maillard browning kinetics in a liquid model system, *J. Agric. Food Chem.*, 1992, **40**(5), 707–713.
- 53 C. W. Gao, J. W. Allen, W. H. Green and R. H. West, Reaction Mechanism Generator: Automatic construction of chemical kinetic mechanisms, *Comput. Phys. Commun.*, 2016, **203**, 212–225.
- 54 K. J. Laidler, The development of the Arrhenius equation, *J. Chem. Educ.*, 1984, **61**(6), 494.
- 55 F. Cheng, G. A. Tompsett, D. V. Fraga Alvarez, C. I. Romo, A. M. McKenna, S. F. Niles, R. K. Nelson, C. M. Reddy, S. Granados-Fócil, A. D. Paulsen, R. Zhang and M. T. Timko, Metal oxide supported Ni-impregnated bifunctional catalysts for controlling char formation and maximizing energy recovery during catalytic hydrothermal liquefaction of food waste, *Sustainable Energy Fuels*, 2021, **5**(4), 941–955.
- 56 N. K. Kaiser, J. P. Quinn, G. T. Blakney, C. L. Hendrickson and A. G. Marshall, A Novel 9.4 Tesla FTICR Mass Spectrometer with Improved Sensitivity, Mass Resolution, and Mass Range, *J. Am. Soc. Mass Spectrom.*, 2011, **22**(8), 1343–1351.
- 57 R. B. Madsen, P. Biller, M. M. Jensen, J. Becker, B. B. Iversen and M. Glasius, Predicting the Chemical Composition of Aqueous Phase from Hydrothermal Liquefaction of Model Compounds and Biomasses, *Energy Fuels*, 2016, **30**(12), 10470–10483.
- 58 R. B. Madsen, P. S. Christensen, K. Houlberg, E. Lappa, A. J. Mørup, M. Klemmer, E. M. Olsen, M. M. Jensen, J. Becker, B. B. Iversen and M. Glasius, Analysis of organic gas phase compounds formed by hydrothermal liquefaction of Dried Distillers Grains with Solubles, *Bioresour. Technol.*, 2015, **192**, 826–830.
- 59 M. Ellersdorfer, Hydrothermal co-liquefaction of *Chlorella vulgaris* with food processing residues, green waste and sewage sludge, *Biomass Bioenergy*, 2020, **142**, 105796.
- 60 J. E. Dander and N. K. Garg, Breaking Amides using Nickel Catalysis, *ACS Catal.*, 2017, **7**(2), 1413–1423.
- 61 J. E. Hodge, Dehydrated Foods, Chemistry of Browning Reactions in Model Systems, *J. Agric. Food Chem.*, 1953, **1**(15), 928–943.
- 62 V. M. Monnier, D. R. Sell, X. Wu and K. Rutter, The prospects of health and longevity from the inhibition of the Maillard reaction in vivo, *Int. Congr. Ser.*, 2002, **1245**, 9–19.
- 63 S. I. F. S. Martins, W. M. F. Jongen and M. A. J. S. van Boekel, A review of Maillard reaction in food and implications to kinetic modelling, *Trends Food Sci. Technol.*, 2000, **11**(9), 364–373.

- 64 B. L. Wedzicha and L. P. Leong, Modelling of the Maillard Reaction: Rate Constants for Individual Steps in the Reaction, in *The Maillard Reaction in Foods and Medicine*, ed. J. O'Brien, H. E. Nursten, M. J. C. Crabbe and J. M. Ames, Woodhead Publishing, 2005, pp. 141–146.
- 65 M. J. S. Dewar, S. Olivella and J. J. P. Stewart, Mechanism of the Diels-Alder reaction: reactions of butadiene with ethylene and cyanoethylenes, *J. Am. Chem. Soc.*, 1986, **108**(19), 5771–5779.
- 66 J. A. Norton, The Diels-Alder Diene Synthesis, *Chem. Rev.*, 1942, **31**(2), 319–523.
- 67 S. Alimoradi, H. Stohr, S. Stagg-Williams and B. Sturm, Effect of temperature on toxicity and biodegradability of dissolved organic nitrogen formed during hydrothermal liquefaction of biomass, *Chemosphere*, 2020, **238**, 124573.
- 68 J. Arun, K. P. Gopinath, P. SundarRajan, R. Malolan and P. AjaySrinivaasan, Hydrothermal liquefaction and pyrolysis of *Amphiroa fragilissima* biomass: Comparative study on oxygen content and storage stability parameters of bio-oil, *Bioresour. Technol. Rep.*, 2020, **11**, 100465.
- 69 K. Azizi, M. Keshavarz Moraveji and H. Abedini Najafabadi, A review on bio-fuel production from microalgal biomass by using pyrolysis method, *Renewable Sustainable Energy Rev.*, 2018, **82**, 3046–3059.
- 70 J. Berg, J. L. Tymoczko and L. Stryer, *Biochemistry*, 5th edn, 2002, <https://www.ncbi.nlm.nih.gov/books/NBK22547/>.
- 71 P. Biller and A. B. Ross, Potential yields and properties of oil from the hydrothermal liquefaction of microalgae with different biochemical content, *Bioresour. Technol.*, 2011, **102**(1), 215–225.
- 72 W. Costanzo, U. Jena, R. Hilten, K. C. Das and J. R. Kastner, Low temperature hydrothermal pretreatment of algae to reduce nitrogen heteroatoms and generate nutrient recycle streams, *Algal Res.*, 2015, **12**, 377–387.
- 73 D. J. Zastrow and P. A. J. In, *Hydrothermal Liquefaction of Food Waste and Model Food Waste Compounds*, AIChE, San Francisco, CA, San Francisco, CA, 2013.
- 74 W. K. Dodds and M. R. Whiles, Chapter 14 - Nitrogen, Sulfur, Phosphorus, and Other Nutrients, in *Freshwater Ecology*, ed. W. K. Dodds and M. R. Whiles, Academic Press, 3rd edn, 2020, pp. 395–424.
- 75 Y. Li, S. Leow, A. C. Fedders, B. K. Sharma, J. S. Guest and T. J. Strathmann, Quantitative multiphase model for hydrothermal liquefaction of algal biomass, *Green Chem.*, 2017, **19**(4), 1163–1174.
- 76 J. Li, Z. Wang, X. Yang, L. Hu, Y. Liu and C. Wang, Evaluate the pyrolysis pathway of glycine and glycyglycine by TG-FTIR, *J. Anal. Appl. Pyrolysis*, 2007, **80**(1), 247–253.
- 77 M. Lucian, M. Volpe, L. Gao, G. Piro, J. L. Goldfarb and L. Fiori, Impact of hydrothermal carbonization conditions on the formation of hydrochars and secondary chars from the organic fraction of municipal solid waste, *Fuel*, 2018, **233**, 257–268.
- 78 L. Sheng, X. Wang and X. Yang, Prediction model of biocrude yield and nitrogen heterocyclic compounds analysis by hydrothermal liquefaction of microalgae with model compounds, *Bioresour. Technol.*, 2018, **247**, 14–20.
- 79 P. Regenass, S. Riché, F. Péron, D. Rognan, M. Hibert, N. Girard and D. Bonnet, A step-economical multicomponent synthesis of 3D-shaped aza-diketopiperazines and their drug-like chemical space analysis, *Org. Biomol. Chem.*, 2016, **14**(37), 8859–8863.
- 80 B. Motavaf and P. E. Savage, Effect of Process Variables on Food Waste Valorization via Hydrothermal Liquefaction, *ACS ES&T Engineering*, 2021, **1**(3), 363–374.
- 81 D. Xu and P. E. Savage, Effect of reaction time and algae loading on water-soluble and insoluble biocrude fractions from hydrothermal liquefaction of algae, *Algal Res.*, 2015, **12**, 60–67.
- 82 P. J. Valdez, M. C. Nelson, H. Y. Wang, X. N. Lin and P. E. Savage, Hydrothermal liquefaction of *Nannochloropsis* sp.: Systematic study of process variables and analysis of the product fractions, *Biomass Bioenergy*, 2012, **46**, 317–331.
- 83 Y. Kida, C. A. Class, A. J. Concepcion, M. T. Timko and W. H. Green, Combining experiment and theory to elucidate the role of supercritical water in sulfide decomposition, *Phys. Chem. Chem. Phys.*, 2014, **16**(20), 9220–9228.